Journal of Materials Chemistry A

ROYAL SOCIETY OF CHEMISTRY

PAPER

View Article Online
View Journal | View Issue

Cite this: J. Mater. Chem. A, 2023, 11, 15301

Strain relaxation and phase regulation in quasi-2D perovskites for efficient solar cells†

Haolin Zhang,[a] Ze Wang,[a] Haoyu Wang,[a] Xianghua Yao,[a] Furong Wang,[a] Shuya Wang,[a] Sai Bai,[b] Jiang Huang,[a] Xiao Luo,*[a] Shuanghong Wu*[a] and Xiaodong Liu*[a]

Branched iso-butylammonium (iso-BA$^+$) tends to form a perfectly vertical crystal orientation and thus is a good choice for spacer cations. Currently, a planar p–i–n structure with PEDOT:PSS as a hole transport layer (HTL) is commonly used for iso-BA based devices. PTAA is a better candidate for hole transport compared to PEDOT:PSS, but iso-BA based perovskite solar cells (PSCs) with a PTAA HTL are rarely reported. In this work, we find that iso-BA based perovskite films prepared on a PTAA HTL have significant tensile strain, which results in the destruction of the PTAA layer after spin-coating the PCBM solution in chlorobenzene (CB) on top of the PTAA/(iso-BA)$_2$MA$_{n-1}$Pb$_n$I$_{3n+1}$ (n = 4) film arising from the CB penetrating through the perovskite layer. To address this issue, we introduce 4-fluoro-phenethylammonium (F-PEA$^+$) as a second spacer cation (SSC), which effectively releases the tensile strain in the perovskite film, thereby preventing the CB penetration. Moreover, the introduction of the F-PEA SSC promotes the formation of large-n phases in the perovskite film, achieving uniform phase distribution. The photo-generated excitons in small-n phases can be efficiently transferred to the adjacent large-n phases, and then the free carriers are transported in an interpenetrating charge transport network constructed by large-n phases, which greatly improves the exciton dissociation and carrier transport in the PSCs. By introducing the F-PEA SSC, we obtain a remarkable PCE of 17.17%, the highest efficiency so far for iso-BA based PSCs. Due to the release of tensile strain and optimization of phase distribution, the stability of the devices is also dramatically improved after introducing the F-PEA SSC.

Received 31st March 2023
Accepted 9th June 2023

DOI: 10.1039/d3ta01935g

rsc.li/materials-a

Xiaodong Liu is currently an Associate Professor at the University of Electronic Science and Technology of China (UESTC). He received his BS (2008) and PhD (2013) degrees from Beijing Jiaotong University under the supervision of Prof. Xurong Xu. During his PhD studies (2010–2012), he was a visiting PhD student in Prof. L. Jay Guo's group at the University of Michigan, Ann Arbor. After graduation, he joined Prof. Yongfang Li's group at Soochow University as a postdoctoral fellow. He has published 28 first/corresponding-author papers. His research interests focus on perovskite/organic solar cells and photodetectors.

Introduction

In the past decade, organic–inorganic hybrid perovskites have been applied in various fields, such as solar cells,[1–6] photodetectors,[7–12] light-emitting diodes,[13–18] lasers,[19–21] *etc.* To date, the power conversion efficiency (PCE) of organic–inorganic hybrid perovskite solar cells (PSCs) has risen rapidly from an initial 3.81% to over 25%. However, the inferior stability against moisture, heat and light limits their commercial application. Quasi-two-dimensional (Q-2D) Ruddlesden–Popper (RP) layered perovskites have attracted tremendous attention in recent years because of their excellent moisture stability.[22–24] The general formula of such 2D RP perovskites is A′$_2$A$_{n-1}$B$_n$X$_{3n+1}$ (n = 1, 2, 3, 4, …), where A′ is an aromatic or aliphatic alkylammonium spacer cation (such as phenethylammonium (PEA$^+$) or butylammonium (BA$^+$)), A is a monovalent cation (such as Cs$^+$, $CH_3NH_3^+$ (MA$^+$), or $(NH_2)_2CH^+$ (FA$^+$)), B is a divalent metal cation (such as Pb^{2+} or Sn^{2+}), X is a halide anion (such as I$^-$, Br$^-$, or Cl$^-$), and n is the layer number of inorganic

[a]School of Optoelectronic Science and Engineering, University of Electronic Science and Technology of China (UESTC), Chengdu 610054, China. E-mail: luox@uestc.edu.cn; shwu@uestc.edu.cn; xdliu@uestc.edu.cn

[b]Institute of Fundamental and Frontier Sciences, University of Electronic Science and Technology of China (UESTC), Chengdu 611731, China

† Electronic supplementary information (ESI) available. See DOI: https://doi.org/10.1039/d3ta01935g

$[BX_6]^{4-}$ octahedral slabs within each quantum well. Many effective strategies, such as additive engineering,[25–28] composition engineering,[29,30] interface engineering,[31,32] solvent engineering[33,34] and post-treatment[35–38] have been applied to increase the PCEs of Q-2D RP PSCs, reaching the highest value of 21.07%.[39] Nevertheless, the PCEs of Q-2D RP PSCs still lag far behind their traditional 3D PSC counterparts.

The preparation of high-quality perovskite thin films with perfect vertical orientation and ideal phase distribution is crucial for achieving high-performance Q-2D RP PSCs.[40,41] Chen *et al.* demonstrated that the branched iso-butylammonium (iso-BA^+) spacer aids to form perovskite phases with more preferred vertical orientation compared to the linear *n*-butylammonium (*n*-BA^+) counterpart, and obtained a higher PCE of 10.63% than that of *n*-BA^+ based devices.[42] Qin *et al.* further improved the PCE of iso-BA^+ based Q-2D PSCs to 15% using a p–i–n planar device architecture with PEDOT:PSS as a hole transport layer (HTL).[43] PTAA is a better candidate for hole transport compared to PEDOT:PSS,[44,45] but iso-BA based Q-2D PSCs with a PTAA HTL are rarely reported.[42,43,46–48]

In this work, we find that the iso-BA based perovskite film prepared on the PTAA HTL has substantial tensile strain, which results in the destruction of the PTAA layer after spin-coating the PCBM solution in chlorobenzene (CB) on top of the PTAA/$(iso\text{-}BA)_2MA_{n-1}Pb_nI_{3n+1}$ ($n = 4$) film, resulting from the CB penetrating through the perovskite layer. After introducing 4-fluoro-phenethylammonium (F-PEA^+) as a second spacer cation (SSC), the residual tensile strain in the perovskite film is greatly released, which leads to the prevention of the CB penetration through the perovskite film and inhibition of subsequent re-dissolution of the PTAA layer. Furthermore, the F-PEA SSC promotes the formation of large-*n* phases in the perovskite film, achieving uniform *n*-phase distribution. The excitons generated in small-*n* phases can be efficiently transferred to the adjacent large-*n* phases, and then the free carriers are transported through high-conducting channels formed by large-*n* phases, which greatly improves the exciton dissociation and carrier transport in the PSCs. The combination of the above raises the PCE of Q-2D RP PSCs from 6.28% to 17.17%, which is the highest efficiency so far for iso-BA based Q-2D PSCs (see Table S1†).

Results and discussion

Surface morphology and crystal structure

We first analyse the effect of F-PEA SSC on perovskite film morphology using scanning electron microscopy (SEM). For the sake of convenient description, the Q-2D $(iso\text{-}BA)_{1-x}(F\text{-}PEA)_x$ based perovskite with the optimal ratio of $x = 0.1$ is abbreviated as iso-BA:F-PEA based perovskite hereafter, except for the special statement. Fig. 1a–c show the cross-sectional SEM images of the perovskite films based on pure iso-BA ($x = 0$), iso-BA:F-PEA ($x = 0.1$), and pure F-PEA ($x = 1$) spacers. Among the three perovskite films, the iso-BA:F-PEA based film exhibits the best morphology and crystallinity with the largest grain size, fewest defects and vertically orientated grain boundaries. From

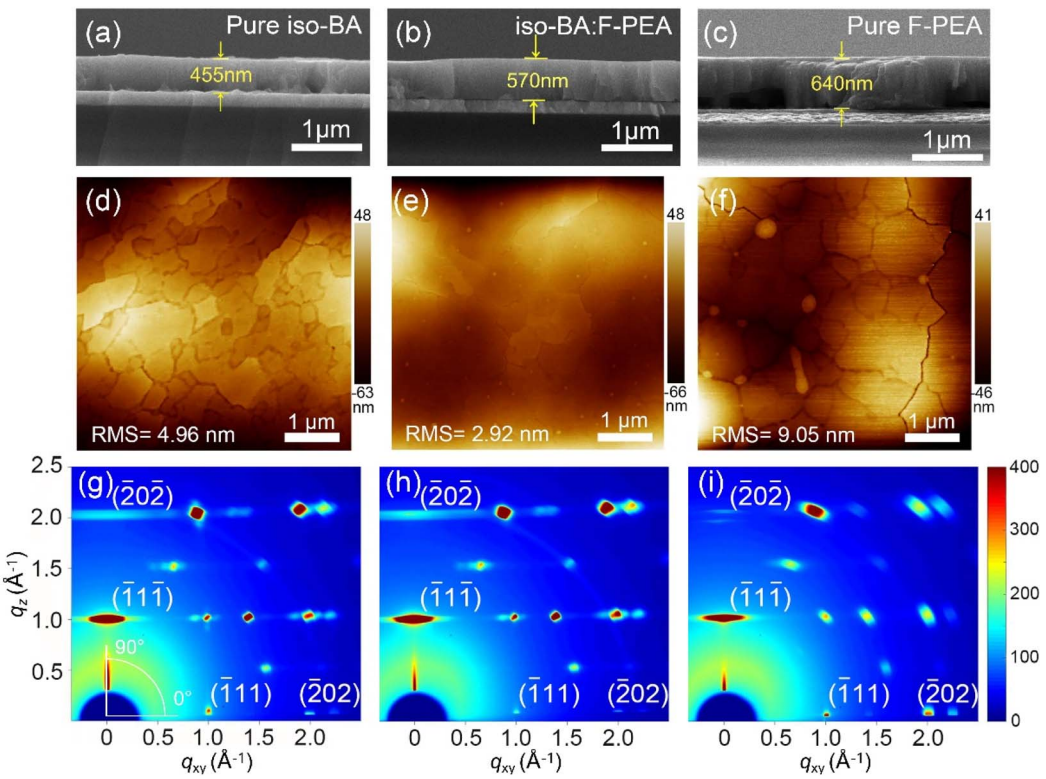

Fig. 1 (a–c) Cross-sectional SEM images, (d–f) top-view AFM height images, and (g–i) GIWAXS patterns of the perovskite films based on (a, d and g) pure iso-BA, (b, e and h) iso-BA:F-PEA, and (c, f and i) pure F-PEA spacers.

their corresponding top-view SEM images (Fig. S1†), all three perovskite films show compact, uniform and smooth surface morphology. The root-mean-square (RMS) roughness values of the perovskite films were estimated from atomic force microscopy (AFM) images (Fig. 1d–f). The iso-BA:F-PEA based perovskite film has the smallest surface roughness of 2.92 nm compared to other perovskite films based on pure iso-BA (4.96 nm) and pure F-PEA spacers (9.05 nm), which is believed to benefit the interfacial contact between the perovskite and PCBM electron transport layer (ETL).

Grazing-incidence wide-angle X-ray scattering (GIWAXS) measurements were conducted to examine the crystallographic orientation of these Q-2D perovskite films (Fig. 1g–i). All the films exhibit sharp and discrete Bragg spots, especially for the (111) and (202) planes, which indicate highly ordered orientation. Noticeably, the iso-BA:F-PEA based perovskite film shows weakened diffraction peaks at an azimuth angle of around 0° for (111) and (202) planes compared to the pure iso-BA and pure F-PEA based perovskite films, suggesting that the orientation of the iso-BA:F-PEA based film is almost perfectly perpendicular to the substrate. The vertically oriented perovskite film is prerequisite for achieving high-performance Q-2D RP PSCs.

Fig. S2† presents the X-ray diffraction (XRD) patterns of Q-2D perovskite films based on pure iso-BA, pure F-PEA, and $(iso\text{-}BA)_{1-x}(F\text{-}PEA)_x$ with different x values. All the perovskite films show two dominant diffraction peaks at about 14.2° and 28.4°, corresponding to the crystallographic planes of (111) and (202), respectively. The intensity ratio between (202) and (111) peaks ($I_{(202)}/I_{(111)}$) is 5.10 for the pure iso-BA based perovskite film, which is remarkably higher than that (0.40) for the pure F-PEA based film. This indicates more preferred vertical orientation for the pure iso-BA based perovskite film than the pure F-PEA based film considering that the (202) peak implies the crystallographic planes aligning perfectly perpendicular to the substrate, while the (111) orientation produces a tilted vertical alignment.[49,50] For $(iso\text{-}BA)_{1-x}(F\text{-}PEA)_x$ based perovskite films, the intensity of the (202) peak gradually decreases with increasing x concurrent with the increase in the intensity of the (111) peak, which results in a monotonic decrease in the $I_{(202)}/I_{(111)}$. This is unfavourable for vertical charge transport. In addition, both (111) and (202) peaks gradually shift towards higher angles with increasing x, which suggests the subtle decrease of crystalline interplanar spacing resulting from the relaxation of tensile strain (as will be discussed later).

Relaxation of tensile strain after F-PEA SSC incorporation

It is interesting to note that when the PCBM solution in chlorobenzene (CB) or pure CB solvent was spin-coated on top of the ITO/PTAA/$(iso\text{-}BA)_2MA_3Pb_4I_{13}$ film, some cracks appear on the top surface (Fig. S3†). Amazingly, this phenomenon disappears when F-PEA partially replaces iso-BA with a ratio of 10% (Fig. S3†). Considering that PTAA is dissolved in CB, we speculate that the cracks in the pure iso-BA based perovskite film

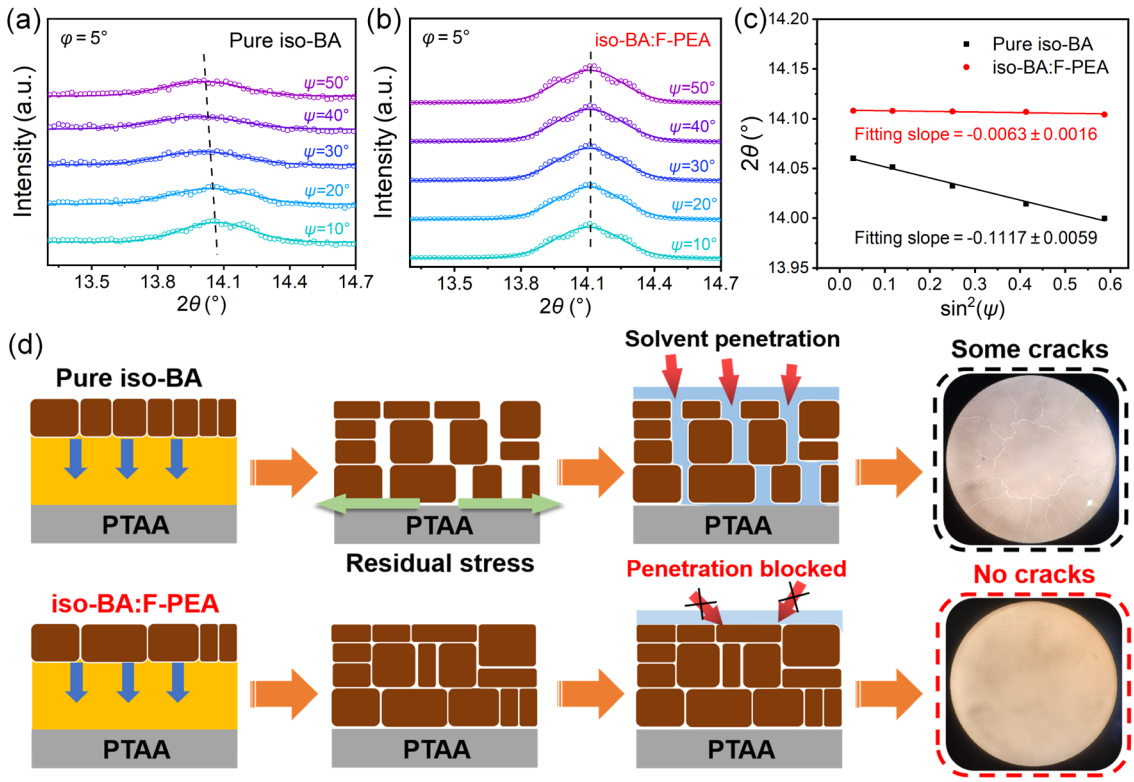

Fig. 2 GIXRD patterns at different instrument tilt angles for (a) pure iso-BA and (b) iso-BA:F-PEA based perovskite films. (c) Linear fit of $2\theta-\sin^2(\Psi)$ of these two perovskite films. (d) Schematic illustration of strain relaxation, prevention of CB penetration through the perovskite film, and inhibition of re-dissolution of the PTAA layer *via* introducing the F-PEA SSC.

can be attributed to the damaged PTAA layer caused by CB solvent penetrating through the perovskite film. In contrast, no cracks are observed in the iso-BA:F-PEA based perovskite film, which indicates that CB penetration is hindered and thus the PTAA layer is not affected. To verify this speculation, we spin coated pure CB on top of the ITO/PEDOT:PSS/$(iso\text{-}BA)_2MA_3Pb_4I_{13}$ film, and no observable cracks are seen on the surface since PEDOT:PSS is insoluble in CB (Fig. S4†).

To explain this phenomenon, we investigate the effect of F-PEA SSC incorporation on the residual strain in the perovskite film by employing the grazing incident X-ray diffraction (GIXRD) technique with the 2θ–$\sin^2(\Psi)$ method.[40] And we choose the characteristic peak at $2\theta \approx 14.2°$, corresponding to the (111) plane, to conduct further analysis. Fig. 2a and b show the GIXRD patterns at different instrument tilt angles (Ψ) for pure iso-BA and iso-BA:F-PEA based perovskite films. By varying Ψ from 10° to 50°, the position of the characteristic peak gradually shifts to lower 2θ, suggesting the increase of crystal plane distance $d_{(111)}$ for the pure iso-BA based film. This indicates that the film based on the pure iso-BA spacer is bearing a large tensile strain. In contrast, the characteristic peak position is almost unchanged with increasing Ψ for the iso-BA:F-PEA based perovskite film, implying negligible residual stress. Fig. 2c shows the linear fit of 2θ–$\sin^2(\Psi)$ for both films. Generally, $\sin^2(\Psi)$ has a linear relationship with 2θ, and the negative slope of the fitting line indicates the existence of tensile stress in the perovskite film. The perovskite film based on the iso-BA:F-PEA spacer exhibits a much smaller slope (0.0063) than that based on the pure iso-BA spacer (0.1117), indicating a significantly reduced tensile strain after introducing the F-PEA SSC.

To further prove the released strain after F-PEA incorporation, we carried out peak force quantitative nanomechanical AFM (PFQNM-AFM) to determine the Young's modulus of both films. As shown in Fig. S5 and Table S2,† the Young's modulus of the iso-BA:F-PEA based perovskite film is 7.819 GPa, which is much lower than that of the pure iso-BA based film (22.016 GPa). The decreased Young's modulus proves the efficient strain relaxation after introducing the F-PEA SSC.[51] Fig. 2d displays a schematic illustration of the tensile stress relaxation, which leads to the formation of a more compact perovskite film with fewer defects. This can explain the inhibition of the CB penetration through the perovskite film after introducing the F-PEA SSC.

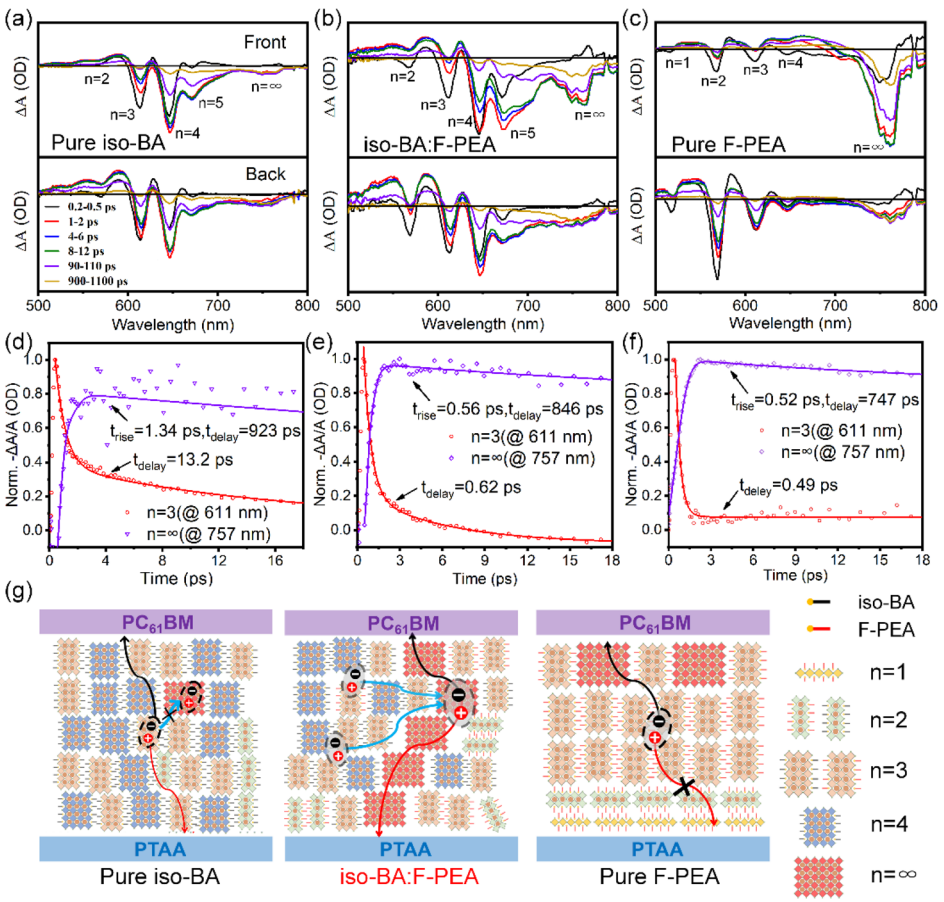

Fig. 3 (a–c) TA spectra at various delay times of (a) pure iso-BA, (b) iso-BA:F-PEA and (c) pure F-PEA based perovskite films under front and back excitations. (d–f) Normalized TA kinetics probed at $n = 3$ (red) and $n \approx \infty$ (purple) phases under front excitation for (d) pure iso-BA, (e) iso-BA:F-PEA and (f) pure F-PEA based perovskite films. (g) Schematic diagrams of phase composition and distribution as well as internal charge transfer between different n phases in pure iso-BA, iso-BA:F-PEA and pure F-PEA based perovskite films.

Phase composition and distribution in Q-2D perovskite films

Fig. S6† shows the absorption spectra of Q-2D perovskite films based on pure iso-BA, iso-BA:F-PEA, and pure F-PEA spacers. All the perovskite films exhibit three sharp absorption peaks at about 566, 611, and 645 nm, corresponding to the excitonic absorption of 2D perovskites with $n = 2$, 3, and 4, respectively. Note that the pure iso-BA based perovskite film has no absorption band in the long-wavelength region from 660 to 750 nm, related to the large-n phases. In contrast, a sharp absorption onset at *ca.* 775 nm is clearly observed for the $(\text{iso-BA})_{1-x}(\text{F-PEA})_x$ based perovskite films with $x \geq 0.5$, which indicates that the introduction of the F-PEA SSC facilitates the formation of 3D-like perovskites.

To verify this speculation, we perform transient absorption (TA) measurements on the perovskite films based on pure iso-BA, iso-BA:F-PEA, and pure F-PEA spacers. Fig. 3a–c show the TA spectra at various delay times of these three perovskite films, under front (*i.e.*, perovskite film side) and back (*i.e.*, glass substrate side) excitations. The pure iso-BA based perovskite film, excited from both front and back sides, exhibits identical spectra (Fig. 3a). Two distinct photobleaching (PB) peaks at *ca.* 611 and 645 nm, assigned to $n = 3$ and 4 phases, are observed for the pure iso-BA based film. Besides, we also detect two small PB peaks at *ca.* 566 and 660 nm corresponding to $n = 2$ and 5 phases. It is notable that the PB signal at *ca.* 755 nm, coming from large-n phases, is very weak, which confirms a negligible amount of 3D-like perovskites in the pure iso-BA based film. In contrast, the iso-BA:F-PEA based film presents multiple perovskite phases with $n = 2$, 3, 4, 5 and $\approx \infty$ under either front or back excitation, which verifies that the F-PEA SSC promotes the formation of large-n phases. Additionally, the small difference between front-excited and back-excited PB signals implies uniform distribution of various n phases in the whole iso-BA:F-PEA based perovskite film. Differently, the pure F-PEA based perovskite film displays a dominant PB peak contributed from large-n phases, and three weak PB peaks attributed to $n = 2$, 3 and 4 phases when excited from the front side. Upon the back excitation, the PB peaks from small-n phases become much stronger, while the intensity of the PB peak from large-n phases is significantly weakened. This indicates the formation of orderly n phase distribution with large-n phases primarily located at the upper surface and small-n phases majorly located at the bottom surface of the pure F-PEA based perovskite film, which is consistent with our previous results.[52] Note that a weak PB peak from the $n = 1$ phase is observed in the pure F-PEA based film under back excitation, which impedes the charge transport considering the horizontal orientation of $n = 1$ 2D perovskite. It should be mentioned that the difference in phase composition and distribution for pure iso-BA, iso-BA:F-PEA, and pure F-PEA based perovskite films may correlate with the solubility of the spacer cation in the DMF:DMSO blend. The solubility values of F-PEAI and iso-BAI are 6.0 and 3.1 mol L^{-1}, respectively. Due to the low solubility of iso-BAI, small-n perovskites tend to nucleate in the initial stage of perovskite formation, which results in the uniform distribution of different n phases. In contrast, owing to the high solubility of F-PEAI, large-n perovskites prefer to nucleate at the early stage of film formation, leading to the ordered n phase distribution.

Phase composition and distribution in Q-2D perovskite films greatly influence the charge transfer and extraction. To probe the internal charge transfer between different n phases, we performed ultrafast TA spectroscopy on pure iso-BA, iso-BA:F-PEA, and pure F-PEA based perovskite films. Fig. 3d–f show the TA kinetics probed at small-n ($n = 3$) and large-n ($n \approx \infty$) phases under front excitation. The kinetics data are fitted with a multiexponential function, and the corresponding fitted parameters are summarized in Table S3.† For the pure iso-BA based perovskite film, TA kinetics at $n = 3$ shows a decay lifetime of 13.2 picoseconds (ps), which is much slower than the rise time of large-n phases (1.34 ps). This indicates inefficient charge transfer from small-n to large-n phases, which can be rationalized by considering that a tiny amount of large-n perovskites exist in the pure iso-BA based film.[52] In contrast, for the iso-BA:F-PEA based perovskite film, the decay lifetime of the $n = 3$ phase is 0.62 ps, comparable to the rise time of large-n phases (0.56 ps), suggesting fast effective energy/charge transfer from small-n to large-n phases.[53] Based on the above TA and GIWAXS results, we depict schematic diagrams to illustrate the proposed phase composition and spatial distribution in the pure iso-BA and iso-BA:F-PEA based perovskite films. As shown in Fig. 3g, both films exhibit uniform vertical distribution of various n phases. However, the pure iso-BA based film contains a tiny amount of 3D-like phases, giving rise to less efficient energy/charge transfer from small-n to large-n phases, while the iso-BA:F-PEA based film possesses a large amount of 3D-like phases, leading to highly efficient energy/charge transfer. Furthermore, abundant 3D-like phases with good conductivity are intercalated with small-n phases to form an interpenetrating network for efficient charge-carrier transport in the iso-BA:F-PEA based film, which is beneficial to enhance the device performance.[54] Different from the uniform phase distribution of pure iso-BA and iso-BA:F-PEA based perovskite films, the pure F-PEA based film exhibits an ordered n phase distribution, which is also considered beneficial for the charge transport by providing an efficient energy-cascade channel. As shown in Fig. 3f, the decay lifetime of $n = 3$ phase (0.49 ps) for the pure F-PEA based perovskite film is quite similar with the rise time of large-n phases (0.52 ps), implying efficient charge transfer from small-n to 3D-like phases. Nevertheless, the presence of the horizontally oriented $n = 1$ phase in the pure F-PEA based film hinders the hole transport and extraction, which is detrimental to the device performance (Fig. 3g).[55]

Device performance and stability

To examine the impact of the F-PEA SSC on the photovoltaic device performance, we fabricated planar p–i–n PSCs with the architecture of ITO/PTAA/Q-2D perovskite/$PC_{61}BM$/PEI/Ag (Fig. 4a), where the $PC_{61}BM$/PEI bilayer is frequently adopted in our laboratory to passivate perovskite surface defects and optimize interfacial energy level alignment. The J–V curves of the champion devices with pure iso-BA, iso-BA:F-PEA, and pure F-PEA based perovskites are shown in Fig. 4b, and the obtained

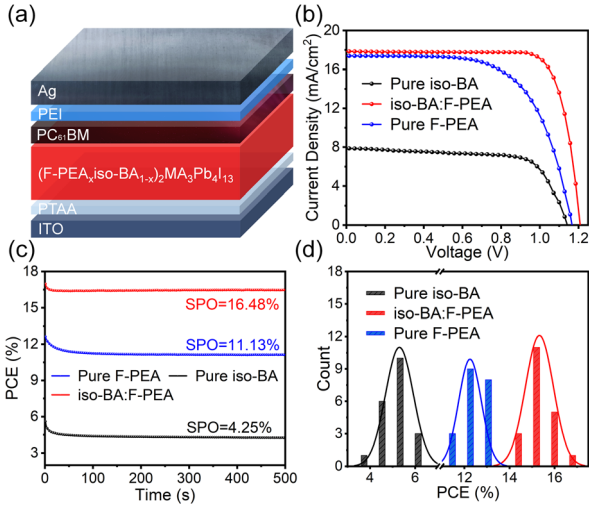

Fig. 4 (a) Device architecture of our Q-2D PSCs. (b) *J–V* curves, (c) steady-state PCEs at the maximum power point, (d) PCE histograms for 20 devices of pure iso-BA, iso-BA:F-PEA and pure F-PEA based PSCs.

photovoltaic parameters are summarized in Table 1. Details on the optimization of F-PEA SSC content for maximizing the device efficiency are presented in Fig. S7 and Table S4,† and the optimal content of F-PEA is 10%. The pure iso-BA based Q-2D PSC exhibits a very low PCE of 6.28% (under the reverse scan), which is mainly attributed to the destruction of the PTAA film by the solvent of PCBM (*i.e.*, CB) arising from the CB penetration through the perovskite film.

After introducing the F-PEA SSC, the CB penetration is prevented due to the released tensile strain in the iso-BA:F-PEA based film. Moreover, the incorporation of the F-PEA SSC improves the perovskite film morphology and provides a more efficient charge-transport channel, which results in a dramatic enhancement in PCE. The iso-BA:F-PEA based PSC delivers a remarkable PCE of 17.17% (under the reverse scan) with the simultaneously increased open-circuit voltage (V_{OC}), short-circuit current density (J_{SC}), and fill factor (FF). This PCE is also higher than that (12.95%) of the pure F-PEA based PSC, which is ascribed to the more vertical crystal orientation in the iso-BA:F-PEA based perovskite film. Fig. S8† shows the external quantum efficiency (EQE) spectra of these three types of PSCs. The iso-BA:F-PEA based device exhibits a significantly improved EQE response over the whole wavelength range compared to the pure iso-BA based device, leading to a dramatic increase in the integrated J_{SC} from 7.77 to 17.30 mA cm^{-2}. Additionally, the EQE curves of the iso-BA:F-PEA and pure F-PEA based devices almost overlap with each other, giving rise to the comparable integrated J_{SC} values. Note that for all these devices, the integrated J_{SC} values from EQE curves agree well with the corresponding J_{SC} values obtained from the *J–V* curves within 3% mismatch (Fig. 4b), indicating the good reliability of our device performance.

Fig. 4c presents the stabilized power output (SPO) under the maximum power point tracking for these three PSCs. The stabilized PCEs for pure iso-BA, iso-BA:F-PEA, and pure F-PEA based devices are 4.25%, 16.48% and 11.13%, respectively, which are consistent with the *J–V* results. To further investigate the hysteresis behaviour of PSCs, we calculate the hysteresis index (HI) with the equation of HI = (PCE_{RS} − PCE_{FS})/PCE_{RS}, where PCE_{RS} and PCE_{FS} represent the PCEs measured under the reverse scan and forward scan, respectively. The pure iso-BA based device exhibits a rather strong hysteresis with a HI of 33.0%. After introducing the F-PEA SSC, the HI is significantly reduced to 6.0%, which is even lower than that (9.1%) of the pure F-PEA based device.[56] Fig. 4d shows the PCE histograms of these PSCs. The iso-BA:F-PEA based devices exhibit a narrow PCE distribution with a high average value, suggesting very good reproducibility.

The light intensity (P_{light}) dependence of J_{SC} and V_{OC} was measured to further investigate the charge-carrier recombination kinetics in Q-2D PSCs. Fig. S9† shows the near-linear dependence of J_{SC} on the P_{light} for the pure iso-BA, iso-BA:F-PEA, and pure F-PEA based devices. The J_{SC} has a power-law relationship with the P_{light}: $J_{SC} \propto (P_{light})^{\beta}$, where β is the power-law component that will approach 1 if the bimolecular recombination is negligible.[57] The extracted β values are 0.95, 0.99 and 0.96 for the devices based on pure iso-BA, iso-BA:F-PEA, and pure F-PEA spacers, respectively, which indicates more efficient sweep-out of charge carrier and considerably reduced bimolecular recombination under short-circuit condition after the incorporation of the F-PEA SSC. Fig. 5a presents the semilogarithmic plot of V_{OC} *versus* P_{light} for the three devices. The relationship of V_{OC} and P_{light} can be expressed as $V_{OC} \propto n(k_BT/q)\ln(P_{light})$, where n, k_B, T, and q represent the ideal factor, the Boltzmann

Table 1 Photovoltaic parameters of the champion Q-2D PSCs based on pure iso-BA, iso-BA:F-PEA and pure F-PEA spacer cations. RS and FS stand for the reverse scan (from open circuit to short circuit) and forward scan (from short circuit to open circuit), respectively

Spacer cation	Scan direction	V_{OC} (V)	J_{SC} (mA cm^{-2})	FF (%)	PCE (%)	J_{SC}[a] (mA cm^{-2})	HI[b] (%)
iso-BA	RS	1.14	7.94	69.3	6.28	7.77	33.0
	FS	1.11	8.03	47.3	4.21		
iso-BA:F-PEA	RS	1.21	17.77	79.9	17.17	17.30	6.0
	FS	1.19	18.01	75.4	16.14		
F-PEA	RS	1.17	17.38	63.9	12.95	16.97	9.1
	FS	1.14	17.61	58.4	11.77		

[a] The J_{SC} is integrated from the EQE curve over the entire solar spectrum. [b] The HI is calculated using the equation HI = (PCE_{RS} − PCE_{FS})/PCE_{RS}.

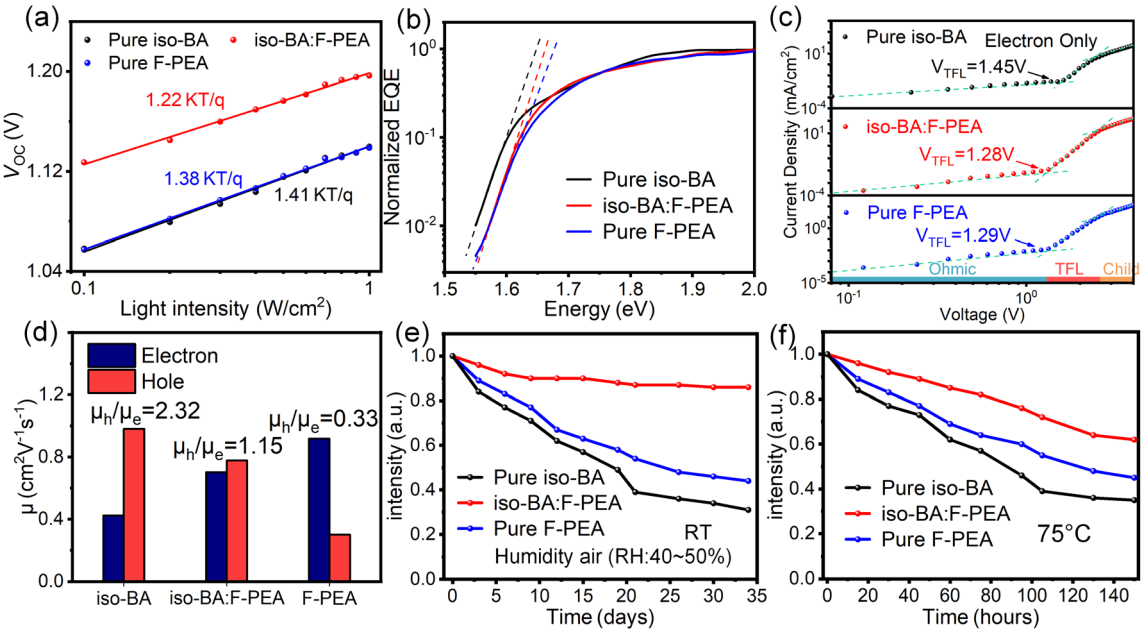

Fig. 5 (a) P_{light} dependent V_{OC} plots for pure iso-BA, iso-BA:F-PEA, and pure F-PEA based PSCs. (b) Urbach energy calculated from EQE curves. (c) Dark J–V curves of electron-only devices based on pure iso-BA, iso-BA:F-PEA, and pure F-PEA based perovskites. (d) Electron and hole mobilities extracted from the corresponding single carrier devices. (e) Humidity stability of unencapsulated devices based on these three perovskites at RT and 45 ± 5% RH. (f) Thermal stability of unencapsulated devices measured at 75 °C in a nitrogen glovebox.

constant, the absolute temperature and the unit charge, respectively. The n value is an indicator of the dominant recombination mechanism in PSCs, and it should be unity if trap-assisted recombination is negligible under open-circuit conditions.[57] The extracted n values for the pure iso-BA, iso-BA:F-PEA, and pure F-PEA based devices are 1.41, 1.22 and 1.38, respectively, implying a reduced trap-assisted recombination after introducing the F-PEA SSC.

By fitting the Urbach tail, we investigate the effect of introducing the F-PEA SSC on the degree of electronic disorder of perovskite films.[58] We calculate the Urbach energy (E_U) from the EQE curves of PSCs (Fig. 5b) according to the following equation:

$$\alpha = \alpha_0 \exp\left(\frac{E - E_g}{E_U}\right)$$

where α is the absorption coefficient, α_0 is a material constant, E is the photon energy, and E_g is the bandgap energy.[59] The values of E_U are determined to be 21.28, 20.05 and 22.37 meV for pure iso-BA, iso-BA:F-PEA, and pure F-PEA based perovskite films, respectively. The smallest E_U of the iso-BA:F-PEA based film suggests the lowest electronic disorder, which results in the reduced voltage loss. To quantitatively assess the trap-density (N_t) and charge carrier mobility in the perovskite films, we performed space-charge-limited current (SCLC) measurements on the electron-only devices with the structure of ITO/SnO_2/Q-2D perovskite/PCBM/Ag and hole-only devices with the structure of ITO/PTAA/Q-2D perovskite/spiro-TTB/Ag. The N_t is determined from trap-filled limit voltage (V_{TFL}) according to the following equation:

$$N_t = \frac{2\varepsilon_0\varepsilon_r V_{TFL}}{qd^2}$$

where ε_0 is the vacuum permittivity, ε_r is the relative dielectric constant of the perovskite, and d is the thickness of the perovskite film. The extracted V_{TFL} values of electron-only devices based on pure iso-BA, iso-BA:F-PEA, and pure F-PEA spacers are 1.45, 1.28 and 1.29 V, yielding the electron trap state densities ($N_{t,e}$) of 1.28×10^{16}, 1.13×10^{16} and 1.14×10^{16} cm^{-3}, respectively (Fig. 5c). The $N_{t,e}$ is notably reduced after introducing the F-PEA SSC. The estimated hole trap state density ($N_{t,h}$) values of pure iso-BA, iso-BA:F-PEA, and pure F-PEA based devices are 1.04×10^{16}, 1.07×10^{16} and 1.89×10^{16} cm^{-3}, respectively (Fig. S10†). The $N_{t,e}$ of the iso-BA:F-PEA based film is comparable to that of the pure iso-BA based film, but much lower than that of the pure F-PEA based film. The electron (μ_e) and hole (μ_h) mobilities are estimated from the SCLC method using the Mott–Gurney equation. The calculated μ_e values of pure iso-BA, iso-BA:F-PEA, and pure F-PEA based films are 0.312, 0.703 and 0.918 cm^2 V^{-1} s^{-1}, respectively, and the corresponding μ_h values are 0.981, 0.778 and 0.300 cm^2 V^{-1} s^{-1}, respectively. The μ_h/μ_e of the perovskite film decreases dramatically from 2.32 to 1.15 after introducing the F-PEA SSC (Fig. 5d), which indicates more balanced electron and hole transport in iso-BA:F-PEA based PSCs.

Finally, we study the effects of introducing the F-PEA SSC on the stability of Q-2D PSCs. We first test the humidity stability of the non-encapsulated devices under 45 ± 5% relative humidity (RH) at room temperature (RT), and the normalized PCE as a function of aging time is presented in Fig. 5e. The iso-BA:F-PEA based PSC exhibits notably improved humidity stability,

retaining 85% of its initial PCE after 30 days, while the pure iso-BA and pure F-PEA based devices keep only 32% and 45% of their initial PCE values, respectively. Zuo *et al.* reported iso-BA based Q-2D PSCs with a PCE of 16.0%, and tested the stability of the encapsulated devices under 1-sun illumination in air (40 °C temperature, 30–40% RH).[47] The PCE retains 91% of the initial value after 500 h of continuous 1-sun illumination (Table S1†). Herein, the unencapsulated iso-BA:F-PEA based device maintains 85% of the initial PCE after 30 days, indicating its good moisture stability. The excellent moisture resistance of the iso-BA:F-PEA based film is verified by its water contact angle. As shown in Fig. S11,† the contact angle increases from 55° and 54° for pure iso-BA and pure F-PEA based films to 65° for the iso-BA:F-PEA based film, indicating the enhanced hydrophobicity after introducing the F-PEA SSC. The larger water contact angle of the iso-BA:F-PEA based film than the pure F-PEA based film can be attributed to the existence of more small-*n* phases at the upper surface of the iso-BA:F-PEA based film, as evidenced by TA spectra (Fig. 3b and c). For thermal stability, the iso-BA:F-PEA based device maintains 63% of its initial PCE after 150 hours of heating at 75 °C (Fig. 5f), which is better than those of the pure iso-BA (38%) and pure F-PEA (47%) based devices. However, the thermal stability of our iso-BA:F-PEA based devices is still unsatisfactory because the studied perovskite (iso-BA:F-PEA)$_2$MA$_3$Pb$_4$I$_{13}$ consists of the volatile MA^+ components.[39] Further work is ongoing to improve the thermal stability of iso-BA:F-PEA based PSCs by replacing MA^+ with FA^+ cations.

Conclusions

In conclusion, by introducing the F-PEA SSC, the residual strain in the iso-BA based perovskite film is greatly released while the perfectly vertical crystal orientation is maintained. This results in the prevention of the CB penetration through the perovskite film during spin-coating of the PCBM ETL, which further inhibits re-dissolution of the underlying PTAA layer. Furthermore, the introduction of the F-PEA SSC significantly increases the large-*n* phases in the perovskite film, forming a uniform distribution of different *n* phases. Excitons generated in the small-*n* phases are efficiently transferred by energy/charge transfer to the adjacent large-*n* phases, and then the free carriers are transported in an interpenetrating charge transport network formed by large-*n* phases, remarkably improving the exciton dissociation and carrier transport in the PSCs. As a result, the iso-BA:F-PEA based perovskite film shows vertical crystal orientation, ideal uniform phase distribution, balanced charge-carrier transport, and low defect density, yielding a significantly improved PCE of 17.17%. More importantly, the iso-BA:F-PEA based device exhibits obviously enhanced humidity and thermal stability due to the enhancement of hydrophobicity after introducing the F-PEA SSC.

Author contributions

Haolin Zhang: conceptualization, data curation, investigation, formal analysis, and writing – original draft; Ze Wang: investigation and data curation; Haoyu Wang: formal analysis and data curation; Xianghua Yao: data curation; Furong Wang: investigation; Shuya Wang: formal analysis; Sai Bai: formal analysis and validation; Jiang Huang: validation; Xiao Luo: data curation and validation; Shuanghong Wu: funding acquisition, supervision, and writing – review & editing; Xiaodong Liu: funding acquisition, supervision, and writing – review & editing.

Conflicts of interest

There are no conflicts to declare.

Acknowledgements

This work was funded by Grant SCITLAB (No. 20012) of Intelligent Terminal Key Laboratory of Sichuan Province, the National Natural Science Foundation of China (no. 62274024, 61604101 and 61871031), the National Key R&D Program (grant no. 2018YFA0307400), Key-Area Research and Development Program of Guangdong Province (grant no. 20190158) and the Fundamental Research Funds for the Central Universities (no. ZYGX2021YGCX012).

Notes and references

1 D. Zhao, C. Wang, Z. Song, Y. Yu, C. Chen, X. Zhao, K. Zhu and Y. Yan, *ACS Energy Lett.*, 2018, **3**, 305–306.
2 M. A. R. Laskar, W. Luo, N. Ghimire, A. H. Chowdhury, B. Bahrami, A. Gurung, K. M. Reza, R. Pathak, R. S. Bobba, B. S. Lamsal, K. Chen, M. T. Rahman, S. I. Rahman, K. Emshadi, T. Xu, M. Liang, W. H. Zhang and Q. Qiao, *Adv. Funct. Mater.*, 2020, **30**, 2000778.
3 X. Ding, H. Wang, C. Chen, H. Li, Y. Tian, Q. Li, C. Wu, L. Ding, X. Yang and M. Cheng, *Chem. Eng. J.*, 2021, **410**, 128328.
4 J. Jeong, M. Kim, J. Seo, H. Lu, P. Ahlawat, A. Mishra, Y. Yang, M. A. Hope, F. T. Eickemeyer, M. Kim, Y. J. Yoon, I. W. Choi, B. P. Darwich, S. J. Choi, Y. Jo, J. H. Lee, B. Walker, S. M. Zakeeruddin, L. Emsley, U. Rothlisberger, A. Hagfeldt, D. S. Kim, M. Gratzel and J. Y. Kim, *Nature*, 2021, **592**, 381–385.
5 J. J. Yoo, G. Seo, M. R. Chua, T. G. Park, Y. Lu, F. Rotermund, Y. K. Kim, C. S. Moon, N. J. Jeon, J. P. Correa-Baena, V. Bulovic, S. S. Shin, M. G. Bawendi and J. Seo, *Nature*, 2021, **590**, 587–593.
6 B. Du, W. Yang, Q. Jiang, H. Shan, D. Luo, B. Li, W. Tang, F. Lin, B. Shen, Q. Gong, X. Zhu, R. Zhu and Z. Fang, *Adv. Opt. Mater.*, 2018, **6**, 1701271.
7 H. Sun, W. Tian, F. Cao, J. Xiong and L. Li, *Adv. Mater.*, 2018, **30**, e1706986.
8 H. Min, D. Y. Lee, J. Kim, G. Kim, K. S. Lee, J. Kim, M. J. Paik, Y. K. Kim, K. S. Kim, M. G. Kim, T. J. Shin and S. Il Seok, *Nature*, 2021, **598**, 444–450.
9 A. Ray, B. Martin-Garcia, A. Moliterni, N. Casati, K. M. Boopathi, D. Spirito, L. Goldoni, M. Prato, C. Giacobbe, C. Giannini, F. Di Stasio, R. Krahne,

L. Manna and A. L. Abdelhady, *Adv. Mater.*, 2022, **34**, e2106160.
10 C. Li, C. Han, Y. Zhang, Z. Zang, M. Wang, X. Tang and J. Du, *Sol. Energy Mater. Sol. Cells*, 2017, **172**, 341–346.
11 D. Liu, B. B. Yu, M. Liao, Z. Jin, L. Zhou, X. Zhang, F. Wang, H. He, T. Gatti and Z. He, *ACS Appl. Mater. Interfaces*, 2020, **12**, 30530–30537.
12 Y. Yue, M. Li, H. Li, N. Chai, Y. Dong, Z. Li, X. Chen and X. Wang, *Chem. Eng. J.*, 2022, **441**, 135997.
13 C.-Y. Chang, A. N. Solodukhin, S.-Y. Liao, K. P. O. Mahesh, C.-L. Hsu, S. A. Ponomarenko, Y. N. Luponosov and Y.-C. Chao, *J. Mater. Chem. C*, 2019, **7**, 8634–8642.
14 W. Feng, K. Lin, W. Li, X. Xiao, J. Lu, C. Yan, X. Liu, L. Xie, C. Tian, D. Wu, K. Wang and Z. Wei, *J. Mater. Chem. A*, 2021, **9**, 11064–11072.
15 Z. Liu, W. Qiu, X. Peng, G. Sun, X. Liu, D. Liu, Z. Li, F. He, C. Shen, Q. Gu, F. Ma, H. L. Yip, L. Hou, Z. Qi and S. J. Su, *Adv. Mater.*, 2021, **33**, e2103268.
16 H. Li, H. Lin, D. Ouyang, C. Yao, C. Li, J. Sun, Y. Song, Y. Wang, Y. Yan, Y. Wang, Q. Dong and W. C. H. Choy, *Adv. Mater.*, 2021, **33**, e2008820.
17 C. Kuang, Z. Hu, Z. Yuan, K. Wen, J. Qing, L. Kobera, S. Abbrent, J. Brus, C. Yin, H. Wang, W. Xu, J. Wang, S. Bai and F. Gao, *Joule*, 2021, **5**, 618–630.
18 H. Wang, X. Gong, D. Zhao, Y.-B. Zhao, S. Wang, J. Zhang, L. Kong, B. Wei, R. Quintero-Bermudez, O. Voznyy, Y. Shang, Z. Ning, Y. Yan, E. H. Sargent and X. Yang, *Joule*, 2020, **4**, 1977–1987.
19 Q. Shang, M. Li, L. Zhao, D. Chen, S. Zhang, S. Chen, P. Gao, C. Shen, J. Xing, G. Xing, B. Shen, X. Liu and Q. Zhang, *Nano Lett.*, 2020, **20**, 6636–6643.
20 Y. Mi, Y. Zhong, Q. Zhang and X. Liu, *Adv. Opt. Mater.*, 2019, **7**, 1900544.
21 X. Xiao, W. Li, Y. Fang, Y. Liu, Y. Shao, S. Yang, J. Zhao, X. Dai, R. Zia and J. Huang, *Nat. Commun.*, 2020, **11**, 2215.
22 X. Jiang, J. Zhang, S. Ahmad, D. Tu, X. Liu, G. Jia, X. Guo and C. Li, *Nano Energy*, 2020, **75**, 104892.
23 P. Liu, N. Han, W. Wang, R. Ran, W. Zhou and Z. Shao, *Adv. Mater.*, 2021, **33**, e2002582.
24 P. Fu, Y. Liu, S. Yu, H. Yin, B. Yang, S. Ahmad, X. Guo and C. Li, *Nano Energy*, 2021, **88**, 106249.
25 Y. Xie, H. Yu, J. Duan, L. Xu and B. Hu, *ACS Appl. Mater. Interfaces*, 2020, **12**, 11190–11196.
26 Y. Yang, C. Liu, O. A. Syzgantseva, M. A. Syzgantseva, S. Ma, Y. Ding, M. Cai, X. Liu, S. Dai and M. K. Nazeeruddin, *Adv. Energy Mater.*, 2020, **11**, 2002966.
27 L. Deng, H. Yang, Z. Liu, X. Yang, Z. Huang, H. Yu, K. Wang and J. Li, *ACS Appl. Energy Mater.*, 2021, **4**, 2856–2863.
28 W. Zhang, X. Wu, J. Zhou, B. Han, X. Liu, Y. Zhang and H. Zhou, *ACS Energy Lett.*, 2022, **7**, 1842–1849.
29 S. Ahmad, P. Fu, S. Yu, Q. Yang, X. Liu, X. Wang, X. Wang, X. Guo and C. Li, *Joule*, 2019, **3**, 794–806.
30 J. Yan, W. Zhang, S. Geng, C. Qiu, Y. Chu, R. Meng, P. Zeng, M. Liu, Z. Xiao and Y. Hu, *Chem. Mater.*, 2022, **35**, 289–294.
31 J. W. Lee, Z. Dai, T. H. Han, C. Choi, S. Y. Chang, S. J. Lee, N. De Marco, H. Zhao, P. Sun, Y. Huang and Y. Yang, *Nat. Commun.*, 2018, **9**, 3021.
32 T. Wang, Y. Dong, J. Guo, Q. Li, Z. Chang, M. Chen, R. Wang and Y. Liu, *Adv. Funct. Mater.*, 2021, **31**, 2107129.
33 C. Ma, M.-F. Lo and C.-S. Lee, *J. Mater. Chem. A*, 2018, **6**, 18871–18876.
34 W. Ke, L. Mao, C. C. Stoumpos, J. Hoffman, I. Spanopoulos, A. D. Mohite and M. G. Kanatzidis, *Adv. Energy Mater.*, 2019, **9**, 1803384.
35 G. Wu, X. Li, J. Zhou, J. Zhang, X. Zhang, X. Leng, P. Wang, M. Chen, D. Zhang, K. Zhao, S. F. Liu, H. Zhou and Y. Zhang, *Adv. Mater.*, 2019, **31**, e1903889.
36 X. Lian, H. Wu, L. Zuo, G. Zhou, X. Wen, Y. Zhang, G. Wu, Z. Xie, H. Zhu and H. Chen, *Adv. Funct. Mater.*, 2020, **30**, 2004188.
37 Y. Huang, Y. Li, E. L. Lim, T. Kong, Y. Zhang, J. Song, A. Hagfeldt and D. Bi, *J. Am. Chem. Soc.*, 2021, **143**, 3911–3917.
38 X. Li, K. Li, B. Wang, X. Zhang, S. Yue, Y. Li, Q. Chen, S. Li, T. Yue, H. Zhou and Y. Zhang, *Adv. Funct. Mater.*, 2021, **31**, 2107675.
39 M. Shao, T. Bie, L. Yang, Y. Gao, X. Jin, F. He, N. Zheng, Y. Yu and X. Zhang, *Adv. Mater.*, 2022, **34**, e2107211.
40 H. Wang, C. Zhu, L. Liu, S. Ma, P. Liu, J. Wu, C. Shi, Q. Du, Y. Hao, S. Xiang, H. Chen, P. Chen, Y. Bai, H. Zhou, Y. Li and Q. Chen, *Adv. Mater.*, 2019, **31**, e1904408.
41 C. Zhu, X. Niu, Y. Fu, N. Li, C. Hu, Y. Chen, X. He, G. Na, P. Liu, H. Zai, Y. Ge, Y. Lu, X. Ke, Y. Bai, S. Yang, P. Chen, Y. Li, M. Sui, L. Zhang, H. Zhou and Q. Chen, *Nat. Commun.*, 2019, **10**, 815.
42 Y. Chen, Y. Sun, J. Peng, W. Zhang, X. Su, K. Zheng, T. Pullerits and Z. Liang, *Adv. Energy Mater.*, 2017, **7**, 1700162.
43 Z. Qin, H. Xue, M. Qin, Y. Li, X. Wu, W. R. Wu, C. J. Su, G. Brocks, S. Tao and X. Lu, *Small*, 2023, **19**, e2206787.
44 C. Xu, Z. Liu and E.-C. Lee, *J. Mater. Chem. C*, 2018, **6**, 6975–6981.
45 Z. Liu, L. Wang, C. Xu, X. Xie and Y. Zhang, *ACS Appl. Energy Mater.*, 2021, **4**, 10574–10583.
46 J. M. Hoffman, C. D. Malliakas, S. Sidhik, I. Hadar, R. McClain, A. D. Mohite and M. G. Kanatzidis, *Chem. Sci.*, 2020, **11**, 12139–12148.
47 C. Zuo, A. D. Scully, W. L. Tan, F. Zheng, K. P. Ghiggino, D. Vak, H. Weerasinghe, C. R. McNeill, D. Angmo, A. S. R. Chesman and M. Gao, *Commun. Mater.*, 2020, **1**, 33.
48 J. Lee, G. Jang, S. Ma, C. U. Lee, J. Son, W. Jeong and J. Moon, *Small*, 2022, **18**, e2202159.
49 C. M. M. Soe, W. Nie, C. C. Stoumpos, H. Tsai, J. C. Blancon, F. Liu, J. Even, T. J. Marks, A. D. Mohite and M. G. Kanatzidis, *Adv. Energy Mater.*, 2017, **8**, 1700979.
50 J. Shi, Y. Gao, X. Gao, Y. Zhang, J. Zhang, X. Jing and M. Shao, *Adv. Mater.*, 2019, **31**, e1901673.
51 Q. Cheng, B. Wang, G. Huang, Y. Li, X. Li, J. Chen, S. Yue, K. Li, H. Zhang, Y. Zhang and H. Zhou, *Angew. Chem., Int. Ed.*, 2022, **61**, e202208264.
52 Z. Wang, Q. Wei, X. Liu, L. Liu, X. Tang, J. Guo, S. Ren, G. Xing, D. Zhao and Y. Zheng, *Adv. Funct. Mater.*, 2020, **31**, 2008404.

53 J. Qing, X.-K. Liu, M. Li, F. Liu, Z. Yuan, E. Tiukalova, Z. Yan, M. Duchamp, S. Chen, Y. Wang, S. Bai, J.-M. Liu, H. J. Snaith, C.-S. Lee, T. C. Sum and F. Gao, *Adv. Energy Mater.*, 2018, **8**, 1800185.
54 J. Zhang, J. Qin, M. Wang, Y. Bai, H. Zou, J. K. Keum, R. Tao, H. Xu, H. Yu, S. Haacke and B. Hu, *Joule*, 2019, **3**, 3061–3071.
55 F. Li, Y. Xie, Y. Hu, M. Long, Y. Zhang, J. Xu, M. Qin, X. Lu and M. Liu, *ACS Energy Lett.*, 2020, **5**, 1422–1429.
56 D. H. Kang and N. G. Park, *Adv. Mater.*, 2019, **31**, e1805214.
57 Z. Wang, L. Liu, X. Liu, D. Song, D. Shi, S. Wu, Y. Tong, H. Ren, M. Li, Y. Zheng and D. Zhao, *Chem. Eng. J.*, 2022, **432**, 134367.
58 X. Lai, W. Li, X. Gu, H. Chen, Y. Zhang, G. Li, R. Zhang, D. Fan, F. He, N. Zheng, J. Yu, R. Chen, A. K. K. Kyaw and X. W. Sun, *Chem. Eng. J.*, 2022, **427**, 130949.
59 S. Wu, Z. Li, J. Zhang, T. Liu, Z. Zhu and A. K. Jen, *Chem. Commun.*, 2019, **55**, 4315–4318.